

Hot electron generation through near-field excitation of plasmonic nanoresonators

Felix Binkowski,¹ Tong Wu,² Philippe Lalanne,² Sven Burger,^{1,3} and Alexander O. Govorov⁴

¹*Zuse Institute Berlin, 14195 Berlin, Germany*

²*LP2N, Institut d'Optique Graduate School, CNRS, Univ. Bordeaux, 33400 Talence, France*

³*JCMwave GmbH, 14050 Berlin, Germany*

⁴*Department of Physics and Astronomy, Ohio University, Athens, Ohio 45701, United States*

We theoretically study hot electron generation through the emission of a dipole source coupled to a nanoresonator on a metal surface. In our hybrid approach, we solve the time-harmonic Maxwell's equations numerically and apply a quantum model to predict the efficiency of hot electron generation. Strongly confined electromagnetic fields and the strong enhancement of hot electron generation at the metal surface are predicted and are further interpreted with the theory of quasinormal modes. In the investigated nanoresonator setup, both the emitting source and the acceptor resonator are localized in the same volume, and this configuration looks promising to achieve high efficiencies of hot electron generation. By comparing with the efficiency calculated in the absence of the plasmonic nanoresonator, that is, the dipole source is located near a flat, unstructured metal surface, we show that the effective excitation of the modes of the nanoresonator boosts the generation efficiency of energetic charge carriers. The proposed scheme can be used in tip-based spectroscopies and other optoelectronic applications.

I. INTRODUCTION

Light-matter interactions in metal nanostructures can be strongly enhanced by plasmonic resonance effects [1, 2]. Hot electron generation, which attracted significant attention in recent years [3–10], is one important effect resulting from the absorption of plasmons by metal surfaces. With this effect, visible light can be harvested and its energy can be transferred to an adjacent semiconductor, where the energy can then be used for photocatalytic processes [11]. The impact of morphology and materials on local field enhancement and hot electron generation is typically investigated in setups with illumination from the far field, e.g., solar illumination and other macroscopic illumination settings [12–14]. However, there are also various types of localized light sources accessible, such as plasmonic tips, single molecules, quantum wells, or quantum dots [15–17], which have so far not been considered for the generation of excited charge carriers.

The efficiency of hot electron generation in metal nanostructures depends on the magnitude of the electric fields in the vicinity of the nanostructures [5]. Nanofabrication technologies allow fabrication of plasmonic nanoresonators of various shape and characteristic size well below 100 nm [18], which enables light confinements at the nanometre scale: The plasmonic resonances of the deep-subwavelength resonators can be efficiently excited by localized emitters resulting in highly localized electromagnetic fields at the metal surfaces [19, 20].

For the design and optimization of nanophotonic devices based on emitter-resonator excitations, modal approaches are a common theoretical tool [21]. The localized surface plasmon resonances of the systems, which are quasinormal modes (QNMs) [21, 22], are electromagnetic field solutions to the time-harmonic source-free Maxwell's equations. The corresponding resonance problems are solved numerically [23], and the solutions allow to obtain insights into the physical properties of the nanophotonic devices.

In this work, we investigate hot electron generation with a localized emitter placed in the near field of a metal nanostructure. In particular, we numerically study a circular nanogroove resonator on a silver surface with a characteristic size of ~ 40 nm and compare the efficiency of hot electron generation in the presence and absence of the nanoresonator. We compute and analyze the hot electron generation with a quantum model assisted by full-wave simulations and further investigate the impact of geometrical parameters. We numerically demonstrate that the excited localized resonance of the nanoresonator leads to an enhancement of the hot electron generation efficiency of more than one order of magnitude compared to the flat surface.

II. EXCITATION OF PLASMONIC RESONANCES WITH LOCALIZED EMITTERS

A. Theoretical background and numerical methods

In nano-optics, in the steady-state regime, the electric fields $\mathbf{E}(\mathbf{r}, \omega_0) \in \mathbb{C}^3$ resulting from a source field are solutions to the time-harmonic Maxwell's equations in second-order form,

$$\nabla \times \mu^{-1} \nabla \times \mathbf{E}(\mathbf{r}, \omega_0) - \omega_0^2 \epsilon(\mathbf{r}, \omega_0) \mathbf{E}(\mathbf{r}, \omega_0) = i\omega_0 \mathbf{J}(\mathbf{r}), \quad (1)$$

This work has been accepted for publication:
F. Binkowski et al., ACS Photonics (2021).
DOI: [10.1021/acsp Photonics.1c00231](https://doi.org/10.1021/acsp Photonics.1c00231)

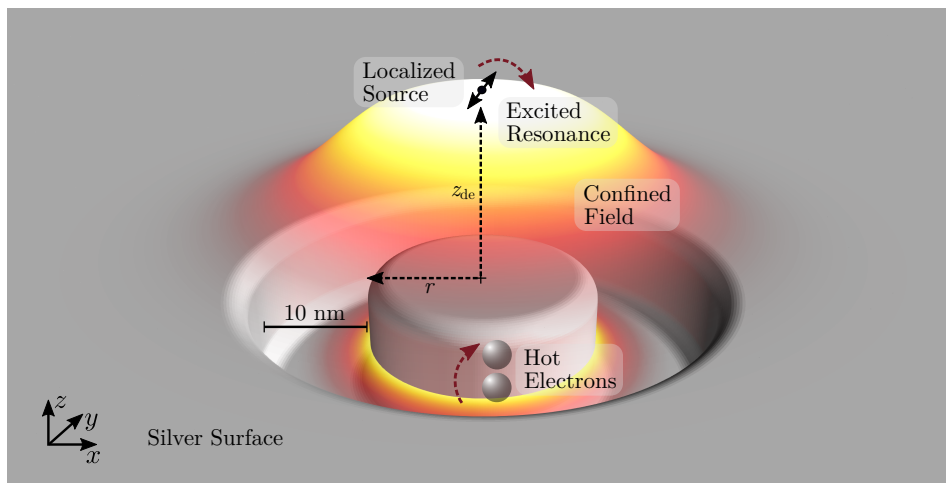


FIG. 1. Circular nanogroove resonator with radius r on a silver surface interacting with a localized emitter placed at the dipole-to-surface distance z_{de} . The sketched electric field intensity $|\tilde{\mathbf{E}}|^2$ corresponds to an excited localized surface plasmon resonance. Placing a dipole emitter close to the metal surface leads to hot electron generation. The coupling of the emitter with the resonance yields high electric field values localized at the nanogroove, which enhances the efficiency of hot electron generation.

k	Ω_k [eV]	σ_k [eV]
1	$3.9173 - 0.06084i$	$0.09267 + 0.01042i$
2	$3.988 - 0.04605i$	$-0.0015342 - 0.062233i$
3	$4.0746 - 0.63141i$	$1.4911 + 0.40655i$
4	$4.6198 - 2.8279i$	$4.2843 + 4.2181i$

TABLE I. Permittivity model for silver. Poles Ω_k and amplitudes σ_k for the generalized Drude-Lorentz model [24] $\epsilon_{\text{metal,bulk}}(\omega_0) = \epsilon_0(\epsilon_\infty - \omega_p^2/(\omega_0^2 + i\gamma_D\omega_0)) + \epsilon_0 \sum_{k=1}^4 [i\sigma_k/(\omega_0 - \Omega_k) + i\sigma_k^*/(\omega_0 + \Omega_k^*)]$, where ϵ_0 is the vacuum permittivity, $\epsilon_\infty = 0.77259$, $\gamma_D = 0.02228$ eV, and $\omega_p = 9.1423$ eV.

where $\omega_0 \in \mathbb{R}$ is the angular frequency, \mathbf{r} is the spatial position, and $\mathbf{J}(\mathbf{r}) \in \mathbb{C}^3$ is the electric current density corresponding to the source. The source field for a localized source can be modeled by a dipole source $\mathbf{J}(\mathbf{r}) = \mathbf{j}\delta(\mathbf{r} - \mathbf{r}')$, where $\delta(\mathbf{r} - \mathbf{r}')$ is the delta distribution, \mathbf{r}' is the position of the emitter, and \mathbf{j} is the dipole amplitude vector. In the optical regime, the permeability tensor μ typically equals the vacuum permeability μ_0 . The permittivity tensor $\epsilon(\mathbf{r}, \omega_0)$ describes the spatial distribution of material and the material dispersion.

We investigate a dipole emitter placed close to a nanoresonator. The nanoresonator is a circular slit on a silver surface with a depth and width of 10 nm. The structure has corner roundings with a radius of 2 nm. Figure 1 shows a sketch of the geometry of the resonant system. The dipole emitter is polarized parallel to the z direction and located on axis above the central nanocylinder at a separation distance z_{de} of the metal surface. For clearly separating the effect of localized resonances supported by the circular nanogroove resonator, we also investigate a second setup: A localized source is placed at z_{de} above a flat, unstructured silver surface. In both

cases, the permittivity of the silver material is described by a generalized Drude-Lorentz model resulting from a rational fit [24, 25] to experimental data [26], see Tab. I. For the investigations, we choose a spectral region in the optical regime, $200 \text{ nm} \leq \lambda_0 \leq 700 \text{ nm}$, with the wavelength $\lambda_0 = 2\pi c/\omega_0$.

To numerically analyze the dipole emitter interacting with the nanoresonator and with the flat surface, we use the finite element method. Scattering and resonance problems are solved by applying the solver JCMSUITE [27]. The solver employs a subtraction field approach for localized sources, adaptive meshing, higher order polynomial ansatz functions, and allows to exploit the rotational symmetry of the geometry [28].

B. Quasinormal mode analysis

When a localized emitter is placed close to a nanostructure, then the optical properties of the system are determined by its underlying resonances. Localized surface plasmon resonances, which are QNMs of the system, are one important resonance phenomena. Figure 1 contains a sketch of a QNM of the nanoresonator which is investigated in this study. QNMs are solutions to Eq. (1) with outgoing wave conditions and without a source field, i.e., $\mathbf{J}(\mathbf{r}) = 0$. We denote the electric and magnetic field distributions of a QNM by $\tilde{\mathbf{E}}(\mathbf{r})$ and $\tilde{\mathbf{H}}(\mathbf{r})$, respectively. The QNMs are characterized by complex eigenfrequencies $\tilde{\omega} \in \mathbb{C}$ with negative imaginary parts. The quality factor Q of a resonance,

$$Q = \frac{\text{Re}(\tilde{\omega})}{-2\text{Im}(\tilde{\omega})},$$

describes its spectral confinement and quantifies the relation between the stored and the dissipated electromag-

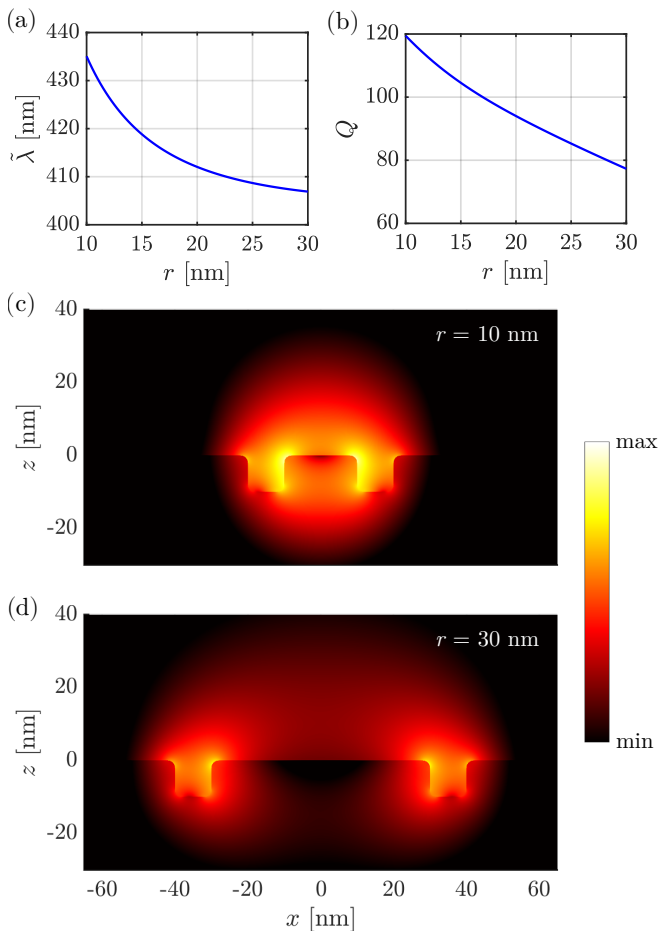


FIG. 2. Simulations of the circular nanogroove resonator supporting one dominant localized resonance in the spectral region of visible light. The associated QNM and its eigenfrequency $\tilde{\omega}$ depend on the radius r of the nanoresonator. The permittivity model $\epsilon_{\text{metal,bulk}}$ given in Tab. I is used. (a,b) Resonance wavelength $\tilde{\lambda} = \text{Re}(2\pi c/\tilde{\omega})$ and quality factor Q of the dominant QNM, respectively. (c) Log-plot (a.u.) of the electric field intensity $|\tilde{\mathbf{E}}|^2$ corresponding to the dominant QNM of the nanoresonator with $r = 10$ nm. The QNM is normalized [29] such that $\int_{\Omega} [\tilde{\mathbf{E}} \cdot \frac{\partial \omega \epsilon}{\partial \omega} \tilde{\mathbf{E}} - \mu_0 \tilde{\mathbf{H}} \cdot \tilde{\mathbf{H}}] dV = 1$, i.e., the map allows a direct estimation and visual comparison of the interaction strength of the mode with point-like unpolarized dipoles. The corresponding eigenfrequency is $\tilde{\omega} = (4.330 - 0.018i) \times 10^{15} \text{ s}^{-1}$ and the resonance wavelength is $\tilde{\lambda} = 435 \text{ nm}$. (d) Log-plot of the electric field intensity of the normalized QNM corresponding to the circular nanogroove resonator with $r = 30$ nm.

netic field energy. In the following section, we investigate how hot electron generation can be increased by the excitation of localized resonances. The physical intuition behind this effect is the following: When a localized source radiating at the frequency ω_0 efficiently couples to a localized resonance, i.e., it is spectrally ($\omega_0 \approx \text{Re}(\tilde{\omega})$) and spatially matched with the resonance, then a large electric field $\mathbf{E}(\omega_0, \mathbf{r})$ around the nanoresonator can be induced by the source. At the resonance frequency $\omega_0 = \text{Re}(\tilde{\omega})$,

the induced field intensity $|\mathbf{E}(\omega_0, \mathbf{r})|^2$ is proportional to Q^2 , which can significantly enhance the hot electron generation. Note that $|\mathbf{E}(\omega_0, \mathbf{r})|^2$ is also proportional to $(\text{Re}(1/\tilde{V}))^2$, where \tilde{V} is the mode volume [29] describing the spatial confinement of the electromagnetic field of a resonance.

In the optical regime, the circular nanogroove resonator sketched in Fig. 1 supports one dominant localized resonance. The resonance wavelength $\tilde{\lambda} = \text{Re}(2\pi c/\tilde{\omega})$ decreases with an increasing circular slit radius r , see Fig. 2(a). Figure 2(b) shows Q , depending on r , where $Q = 120$ can be observed for $r = 10$ nm. Note that, for smaller radii, due to the decreasing radiation loss, the quality factor would increase further. However, we restrict the investigations to $r \geq 10$ nm. Figure 2(c) shows the electric field intensity of the dominant resonance for $r = 10$ nm. The resonance is strongly localized at the circular slit and is characterized by high electric field values inside and close to the metal. Figure 2(d) shows the electric field intensity of the dominant resonance for $r = 30$ nm. It can be observed that, in comparison to the resonance for $r = 10$ nm, the electric field intensity becomes smaller at the metal surface. The ratio between stored and dissipated electromagnetic field energy decreases with an increasing radius. For the following investigations, we consider the circular nanogroove resonator shown in Fig. 2(c), which has a radius of $r = 10$ nm and a quality factor of $Q = 120$.

C. Dipole emission and absorption

To quantify the interaction of the circular nanogroove resonator with a dipole emitter close to the resonator, we investigate the total power emitted by the dipole, which is also called dipole emission. The dipole emission can be computed by

$$p_{\text{de}}(\omega_0) = -\frac{1}{2} \text{Re}(\mathbf{E}^*(\mathbf{r}', \omega_0) \cdot \mathbf{j}),$$

where $\mathbf{E}^*(\mathbf{r}, \omega_0)$ is the complex conjugate of the electric field, \mathbf{r}' is the position of the emitter, and \mathbf{j} is the dipole amplitude vector. The electric field $\mathbf{E}(\mathbf{r}, \omega_0)$ is computed by solving Eq. (1) with a dipole source.

Based on the modal results from the previous subsection, we place the dipole emitter at $z_{\text{de}} = 20$ nm, which is in a spatial region of high electric field intensity of the dominant resonance shown in Fig. 2(c). In this way, the localized resonance of the circular nanogroove resonator has a significant influence on the emission properties of the dipole emitter. Figure 3(a) shows the dipole emission $p_{\text{de}}(\lambda_0)$. In the case of the nanoresonator, the spectrum is characterized by two significant maxima, which are based on different resonance effects: The dipole emitter couples to the dominant localized resonance with the resonance wavelength $\tilde{\lambda} = 435$ nm and it couples also to a continuum of surface plasmons, which are propagating on the metal surface. As expected, the propagating surface

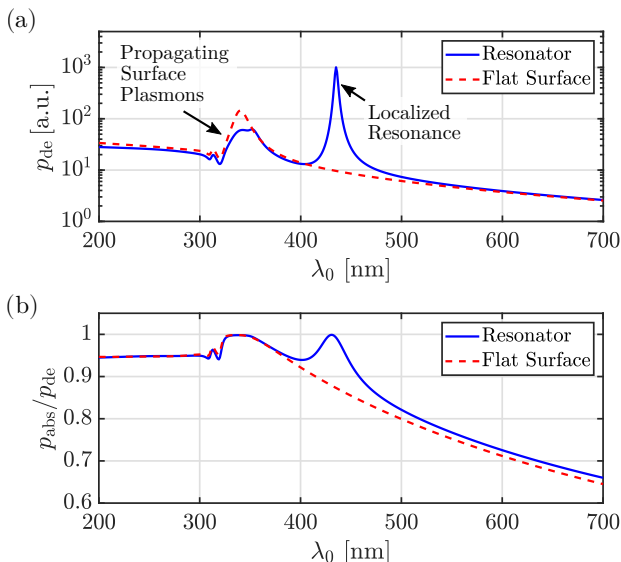


FIG. 3. Simulations of dipole emission and normalized absorption for a localized source placed at the dipole-to-surface distance $z_{de} = 20$ nm. Investigation for the circular nanogroove resonator with $r = 10$ nm and comparison to a flat surface. The permittivity model $\epsilon_{\text{metal,bulk}}$ given in Tab. I is used. (a) Dipole emission p_{de} . (b) Normalized absorption in metal p_{abs}/p_{de} .

plasmons occur not only in the presence of the nanoresonator, but also in the case of the flat surface. Their high density of states give rise to a peak in the spectrum between $\lambda_0 = 300$ nm and $\lambda_0 = 400$ nm, as indicated in Fig. 3(a), where the coupling of the dipole emitter to the propagating surface plasmons is stronger in absence of the nanoresonator.

It can be expected that, for the investigated systems, all energy that is not radiated into the upper hemisphere is absorbed by the metal. Therefore, the total absorbed energy can be computed using the expression

$$p_{\text{abs}}(\omega_0) = p_{de}(\omega_0) - p_{\text{rad}}(\omega_0).$$

The dipole emission radiated into the upper hemisphere, $p_{\text{rad}}(\omega_0)$, is computed by a near-field to far-field transformation and an integration of the Poynting vector over the upper hemisphere. Figure 3(b) shows the absorption $p_{\text{abs}}(\lambda_0)$ normalized by the dipole emission $p_{de}(\lambda_0)$ for $z_{de} = 20$ nm. It can be observed that, close to the wavelength of the localized resonance, most of the energy is absorbed. As the presence of the nanoresonator increases the electromagnetic field energy in the metal, the system with the nanoresonator leads to a higher absorption efficiency than the system with the flat surface.

To summarize, the simulations in this subsection show that a localized source can efficiently excite localized resonances supported by a nanoresonator, as well as propagating surface plasmons on flat metal surfaces. In the following section, it is shown that especially excited localized resonances can have a significant impact on the rate at which hot electrons can be generated in our model system.

III. HOT ELECTRON GENERATION

A. Theoretical background

Considering quantum surface effects in plasmonics, one should start from an elegant theory by Feibelman developed to describe a surface plasmon dispersion in metals [30, 31]. The so-called Feibelman’s d -parameters characterize the dispersion and damping of the surface plasmon mode beyond the classical electromagnetic theory. Furthermore, it was discovered that the plasmon excitations in small nanoparticles experience an additional damping mechanism, the so-called surface-scattering decay [32]. In this quantum mechanism, collective plasmon excitations turn into hot electrons due to scattering at the surfaces [33–38]. A full kinetic picture of the plasmon excitation in a nanostructure involves both low-energy “Drude” electrons forming the coherent plasmon oscillation and the energetic (hot) electrons generated through the surface-assisted Kreibig’s mechanism [39]. The low-energy excitations, regarded above as Drude electrons, can also be derived directly from the quasi-classical theory based on the Boltzmann equation [40, 41]. Another related work, which should be mentioned here, is the theory of hot electron photocurrents generated at metal-semiconductor interfaces [42–45]. In our approach, we combine some of the quantum formalisms mentioned above [33, 38, 39, 45] with the classical formalism of computing the electromagnetic fields at the surfaces by solving Maxwell’s equations. The theoretical treatment below, which incorporates the surface-assisted generation of hot electrons, is very convenient since it allows to investigate nanostructures with arbitrarily complex shapes, in which hot-spot and shape effects determine the formation of plasmonic modes. We note that our formalism does not include a bulk mechanism of hot electron generation due to the electron-phonon scattering [46]. However, such a phonon-assisted channel should not play a dominant role in relatively small nanostructures where plasmonic mode sizes are less than 40 nm [46]. In our case, the groove size of the nanostructure is just 10 nm, and we expect that the leading mechanism is the surface-assisted hot electron generation. Another argument for the importance of the surface-generated hot electrons is that those carriers are created at the surface and, therefore, can be transferred to surface acceptor states for photochemistry or for other detection methods.

B. Quantum efficiency of hot electron generation

The rate of energy dissipation based on the generation of hot electrons at a surface is given by [47]

$$p_{\text{he}}(\omega_0) = \frac{1}{2\pi^2} \frac{e^2 E_F^2}{\hbar} \frac{1}{(\hbar\omega_0)^2} \int_S |\mathbf{E}_n(\mathbf{r}, \omega_0)|^2 dS, \quad (2)$$

where e is the elementary charge, E_F is the Fermi energy, and \hbar is the reduced Planck constant. The normal com-

ponent of the electric field $\mathbf{E}_n(\mathbf{r}, \omega_0)$ is integrated over the surface S . For a detailed derivation of Eq. (2), the reader is referred to ref 47.

The quantum dissipation $p_{\text{he}}(\omega_0)$ is based on optically induced quantum transitions of electrons near to the surface: The energy of photons can be transferred to the electrons because of breaking of linear momentum conservation. This surface scattering effect can be accounted for by a phenomenological approach for metal nanostructures [34, 37, 38]. An additional damping mechanism with the quantum decay parameter γ_s is incorporated in the material model,

$$\epsilon(\omega_0) = \epsilon_{\text{metal,bulk}}(\omega_0) + \epsilon_0 \frac{\omega_p^2}{\omega_0(\omega_0 + i\gamma_D)} - \epsilon_0 \frac{\omega_p^2}{\omega_0(\omega_0 + i(\gamma_D + \gamma_s))}, \quad (3)$$

where $\epsilon_{\text{metal,bulk}}(\omega_0)$ is the permittivity model for the metal bulk material, and ω_p and γ_D are the plasma frequency and the damping constant from the Drude model, respectively, see Tab. I. The quantum decay parameter γ_s describes the broadening due to the scattering of electrons at the surface. For the calculation of γ_s , we consider the total absorption power in a metal nanostructure, given by $p_{\text{abs}} = \text{Im}(\epsilon(\omega_0)) \frac{\omega_0}{2} \int_V \mathbf{E} \cdot \mathbf{E}^* dV$, where $\epsilon(\omega_0)$ is the permittivity model from Eq. (3). It is assumed that $\omega_0^2 \gg (\gamma_D + \gamma_s)^2$, which holds for typical cases in nanophotonics. Applying the resulting simplification $\text{Im}(\epsilon(\omega_0)) \approx \text{Im}(\epsilon_{\text{metal,bulk}}(\omega_0)) + \epsilon_0 \frac{\omega_p^2 \gamma_s}{\omega_0^3}$ and splitting the absorption power p_{abs} into contributions corresponding to bulk and surface effects yield, in particular, the surface-scattering term $p_s = \epsilon_0 \frac{\omega_p^2 \gamma_s}{\omega_0^3} \frac{\omega_0}{2} \int_V \mathbf{E} \cdot \mathbf{E}^* dV$ [37, 38]. This term can be also computed using Eq. (2). The equation $p_{\text{he}} = p_s$ can be transformed and allows to compute the quantum decay parameter γ_s . A corresponding numerical iterative approach is given by [38]

$$\gamma_{s,n} = \frac{3}{4} v_F \frac{\int_S |\mathbf{E}_n(\mathbf{r}, \omega_0, \gamma_{s,n-1})|^2 dS}{\int_V \mathbf{E}(\mathbf{r}, \omega_0, \gamma_{s,n-1}) \cdot \mathbf{E}^*(\mathbf{r}, \omega_0, \gamma_{s,n-1}) dV}, \quad (4)$$

$$n = 0, 1, \dots,$$

where $\gamma_{s,0} = 0$, v_F is the Fermi velocity, and the electric fields are computed by solving Eq. (1) numerically, and subsequently, they are integrated over the surface S and the volume V of the considered nanostructure. For the computation of the electric fields within the iteration, the material model given by Eq. (3) is used. Note that, for $\gamma_{s,0} = 0$, we obtain $\epsilon(\omega_0) = \epsilon_{\text{metal,bulk}}(\omega_0)$ as used for the calculations for the optical problem in the previous section. We further note that a formalism for $\gamma_{s,n}$ can also be derived without the assumption $\omega_0^2 \gg (\gamma_D + \gamma_s)^2$ [38].

The consideration of the quantum decay parameter $\gamma_{s,n}$ is equivalent of solving a self-consistent quantum-classical formalism which fully accounts for the change of the surface response caused by the generation of hot

electrons. With this approach, the total power emitted by a dipole can be expressed as

$$p_{\text{de}}(\omega_0) = p_{\text{abs,bulk}}(\omega_0) + p_{\text{he}}(\omega_0) + p_{\text{rad}}(\omega_0),$$

where $p_{\text{abs,bulk}}(\omega_0)$ is the absorption in the metal bulk. We define the quantum efficiency of hot electron generation as the ratio $\eta_{\text{he}}(\omega_0) = p_{\text{he}}(\omega_0)/p_{\text{de}}(\omega_0)$. This parameter describes the fraction of the dipole energy converted into hot electrons. The efficiency of the absorption in the metal bulk and the radiation efficiency are defined as $\eta_{\text{abs,bulk}}(\omega_0) = p_{\text{abs,bulk}}(\omega_0)/p_{\text{de}}(\omega_0)$ and $\eta_{\text{rad}}(\omega_0) = p_{\text{rad}}(\omega_0)/p_{\text{de}}(\omega_0)$, respectively.

To investigate the effect of hot electron generation for the circular nanogroove resonator, we choose, as in the previous section, the dipole-to-surface distance $z_{\text{de}} = 20$ nm, and solve Eq. (1) with the introduced permittivity model in Eq. (3). The Fermi energy and the Fermi velocity of silver are given by $E_F = 5.48$ eV and $v_F = 1.39 \times 10^6$ m/s [48], respectively. The quantum decay parameter $\gamma_{s,n}$ is obtained by the iteration in Eq. (4), where the abort condition for the iteration is $|\gamma_{s,n} - \gamma_{s,n-1}|/\gamma_{s,n} < 10^{-2}$. For all simulations, with an initial value of $\gamma_{s,0} = 0$, this convergence condition can be achieved within a maximum of four iterations. The electric fields $\mathbf{E}(\mathbf{r}, \omega_0)$ resulting from this procedure are used to compute $p_{\text{de}}(\omega_0)$, $p_{\text{he}}(\omega_0)$, and $p_{\text{rad}}(\omega_0)$. To obtain the absorption in the metal bulk, we use the expression $p_{\text{abs,bulk}}(\omega_0) = p_{\text{de}}(\omega_0) - p_{\text{he}}(\omega_0) - p_{\text{rad}}(\omega_0)$. Note that the quantum decay parameter $\gamma_{s,n}$ and, therefore, the quantum dissipation $p_{\text{de}}(\omega_0)$, depend on the size of the surface S and on the size of the volume V in Eq. (4). For example, for a system radiating at the wavelength of the localized resonance shown in Fig. 2(c), $p_{\text{he}}(\lambda_0 = 435$ nm) changes less than 1% when the radius of the integration domains is doubled from 1 μm to 2 μm . We choose a fixed integration radius of 2 μm for all simulations.

Figure 4(a) shows the computed efficiencies $\eta_{\text{abs,bulk}}(\lambda_0)$, $\eta_{\text{he}}(\lambda_0)$, and $\eta_{\text{rad}}(\lambda_0)$ and the corresponding absolute values for the dipole emission $p_{\text{de}}(\lambda_0)$. In the full spectral range, due to the small dipole-to-surface distance, a large part of the power emitted by the dipole is absorbed in the metal bulk, and only a smaller part is radiated to the upper hemisphere. The quantum efficiency of hot electron generation $\eta_{\text{he}}(\lambda_0)$ is significant in the spectral regions corresponding to the localized resonance shown in Fig. 2(c) and corresponding to the propagating surface plasmons. A comparison of the results for $p_{\text{de}}(\lambda_0)$ in Fig. 4(a) and in Fig. 3(a) shows a slight reduction of $p_{\text{de}}(\lambda_0)$ when the quantum decay parameter $\gamma_{s,n}$ is incorporated in the material model. However, the peaks of $p_{\text{de}}(\lambda_0)$ are still present, which demonstrates that the optical resonance effects are the main drivers for hot electron generation in our model system. In both cases, with and without including the surface-scattering effect in the material model, the maximum of the dipole emission $p_{\text{de}}(\lambda_0)$ is located at the resonance wavelength of the localized resonance, at $\lambda_0 = 435$ nm.

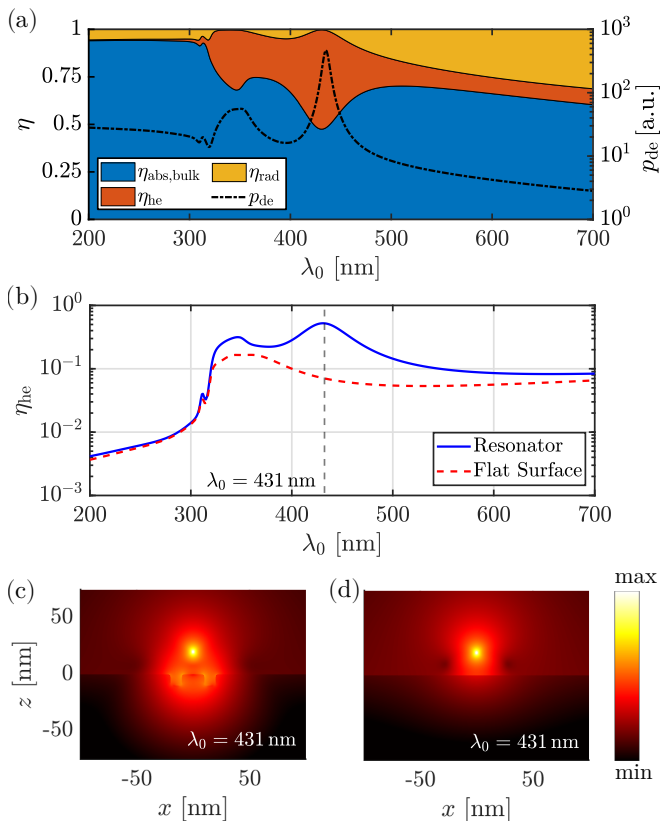


FIG. 4. Simulations of hot electron generation for a localized emitter placed at the dipole-to-surface distance $z_{de} = 20$ nm, for the circular nanogroove resonator with $r = 10$ nm and a flat surface. The modified permittivity function given by Eq. (3) is used. (a) Left y axis: Area plot for the absorption efficiency $\eta_{abs} = p_{abs,bulk}/p_{de}$, hot electron efficiency $\eta_{he} = p_{he}/p_{de}$, and radiation efficiency $\eta_{rad} = p_{rad}/p_{de}$ for the nanoresonator. Right y axis: Dipole emission p_{de} for the nanoresonator. (b) Quantum efficiency of hot electron generation η_{he} for the nanoresonator and a flat surface. (c,d) Log-plot (a.u.) of the electric field intensity $|\mathbf{E}|^2$ resulting from a dipole emitter radiating at the wavelength $\lambda_0 = 431$ nm for the nanoresonator and a flat surface, respectively.

Next, we compare the quantum efficiency in the presence of the nanoresonator with the quantum efficiency for a flat, unstructured surface. Figure 4(b) shows the corresponding spectra $\eta_{he}(\lambda_0)$. In the case of the nanoresonator, the maximum of the quantum efficiency is located close to the resonance wavelength of the localized resonance, and is given by $\eta_{he}(\lambda_0 = 431 \text{ nm}) = 0.52$, which is about one order of magnitude larger than in case of the flat surface. The propagating surface plasmons are responsible for another maximum $\eta_{he}(\lambda_0 = 346 \text{ nm}) = 0.32$. In the case of the flat surface, the quantum efficiency shows one maximum at the wavelength $\lambda_0 = 360$ nm, given by $\eta_{he}(\lambda_0 = 360 \text{ nm}) = 0.17$. The spectra $\eta_{he}(\lambda_0)$ demonstrate that the presence of the nanoresonator has a significant influence on the generation of energetic charge carriers. Figure 4(c) and (d) emphasize this by showing, for the circular nanogroove res-

onator and the flat surface, respectively, the electric field intensities in the vicinity of the dipole emitter radiating at the wavelength $\lambda_0 = 431$ nm, where the quantum efficiency is maximal. The localized source strongly excites the localized resonance of the nanoresonator, which leads to high electric field values at the metal surface enabling enhanced hot electron generation. Note that, close to the wavelength of the localized resonance, the absolute values for the dipole emission $p_{de}(\lambda_0)$ are more than one order of magnitude larger for the system with the nanoresonator than for the system without the nanoresonator, see also Fig. 3(a).

C. Dependence of hot electron generation on emitter placement

Localized light sources can excite resonances that cannot be excited by illumination from the far field, such as dark surface plasmon modes [19] or modes where the overlap integral with the field caused by the far-field illumination is negligible. This allows for additional degrees of freedom in tailoring the light-matter interaction. It can be expected that the position of the dipole emitter in our model system is a degree of freedom that has a significant influence on the generation of excited charge carriers. For investigating this impact, we perform simulations of the hot electron generation with various dipole-to-surface distances. The corresponding results are shown in Figure 5(a). In the full spectral range, with a decreasing dipole-to-surface distance from $z_{de} = 500$ nm to $z_{de} = 10$ nm, the quantum efficiency $\eta_{he}(\lambda_0)$ strongly increases. The most significant effect can be observed at the peak in the spectrum corresponding to the localized resonance. This can be explained through the z_{de} -dependent overlap between localized resonance and source near fields: The resonance excitation and the resulting electromagnetic near fields increase when the dipole-to-surface distance becomes smaller. Note that, below 20 nm, the efficiency at the peak does not further increase significantly with a decrease of the distance. This can be understood by considering that, below 20 nm, almost all emitted energy has already been funneled into the localized resonance, and a further decrease of the distance does not change the electric field distribution near the metal surface. Such a saturation of the hot electron generation efficiency can only be predicted with self-consistent formulas, as given by Eqs. (1), (3), and (4).

Next, we investigate the behavior of the resonance-induced hot electron generation peak by performing a fine sampling of the dipole-to-surface distance z_{de} . Figure 5(b) shows the corresponding dependence of the quantum efficiency η_{he} . In the case of the nanoresonator, the quantum efficiency varies over one order of magnitude, from 3% to 52%, when the distance decreases from 150 nm to 20 nm. In the case of the flat surface, the quantum efficiency only increases from 2% to 7% when the

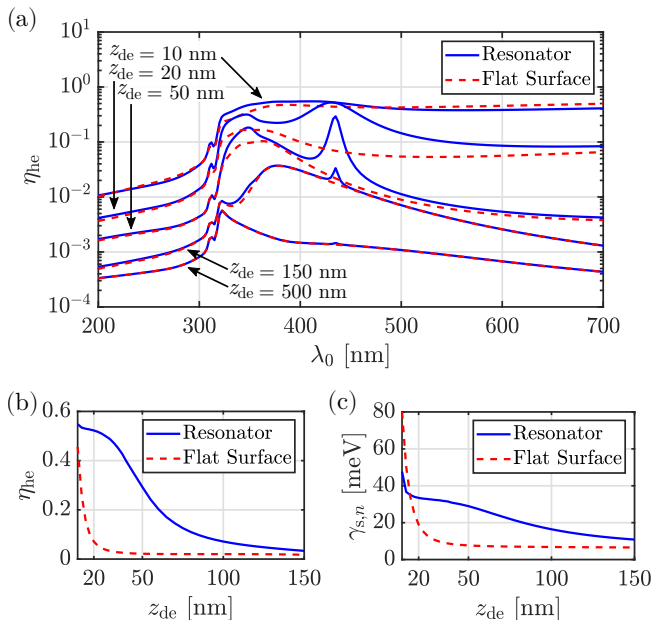


FIG. 5. Simulations of hot electron generation for a localized emitter placed at different dipole-to-surface distances z_{de} , for the circular nanogroove resonator with $r = 10$ nm and a flat surface. The modified permittivity function given by Eq. (3) is used. (a) Quantum efficiency η_{he} as a function of emitter wavelength for various distances z_{de} . (b,c) Quantum efficiency η_{he} and quantum decay parameter $\gamma_{s,n}$, respectively, depending on z_{de} . The number n is the last step of the iteration in Eq. (4). Note that the emitter wavelength changes as z_{de} is varied to match the spectral position of the peak in the spectrum due to the localized resonance. The same wavelength is used for the flat surface.

distance decreases from 150 nm to 20 nm.

By changing the dipole-to-surface distance further, from $z_{de} = 20$ nm to $z_{de} = 10$ nm, an additional significant effect can be observed in the case of the flat surface: The quantum efficiency increases by more than one order of magnitude, up to $\eta_{he} = 0.46$. For such small distances, high- k surface plasmon polaritons can be excited [49]. These high- k surface plasmons have a very small skin depth, which leads to strongly confined electric fields close to the metal surface. This strong effect is not observed when the nanoresonator is present because, in this case, the response is fully dominated by the localized resonance and the energy does not funnel into high- k surface plasmons. As a result, when $z_{de} = 10$ nm, the same order of magnitude of quantum efficiency is obtained in the presence and in the absence of the nanoresonator. Figure 5(c) shows the dependence of the quantum decay parameter $\gamma_{s,n}$ on the distance z_{de} . The quantum dissipation at the surface and the absorption power in the metal bulk are related to the nominator and the denominator in Eq. (4), respectively. For decreasing dipole-to-surface distances, the quantum dissipation increases faster than the absorption in the metal bulk leading to an increase of $\gamma_{s,n}$.

Along with the additional broadening of the plasmon resonance described by $\gamma_{s,n}$, the surface-assisted hot electron generation processes create a peculiar, nonthermal energy distribution of excited electrons inside a driven plasmonic nanocrystal [38, 47]. The computed shapes of nonthermal energy distributions in a nanocrystal can be found in the refs 38 and 47. The intraband hot electrons, which we study here, are generated near the surface, and their spectral generation rate has a nearly-flat distribution in the energy interval $E_F < E < E_F + \hbar\omega_0$. Because of the frequent electron-electron collisions, the high-energy hot electrons experience fast energy relaxation. Therefore, the resulting numbers of hot electrons in the steady states of plasmonic nanostructures are always limited. However, those hot electrons, when generated, have a good chance to be injected into electronic acceptor states at the surface [3, 6, 7, 10, 50, 51]. These electronic acceptors can be in the form of semiconductor clusters (TiO_2) [50, 51] or adsorbed molecular species [7, 10]. Consequently, the injected long-lived hot electrons can cause chemical reactions in a solution [6, 7, 10] or surface growth [52]. Such chemical and shape transformations can be observed in experiments.

Based on the above results, we expect that in potential experimental setups that use hot electron generation by localized sources and nanostructured samples, the significant spectral dependence and position dependence of the generation rate can provide strong experimental signatures and thus can provide guidelines for settings with high-efficiency hot electron generation.

IV. CONCLUSIONS

We analyzed the hot electron generation due to the emission of light by a localized emitter placed in the near field of a metal nanoresonator with electromagnetic field calculations and an approximate quantum model. For a resonant nanostructure on the metal surface, enhanced hot electron generation was observed. This enhancement is based on a plasmonic resonance excited by the emitter. We showed that, for a specific nanoresonator on a silver surface, the quantum efficiency is about one order of magnitude larger than the quantum efficiency of hot electron generation in the case of a flat silver surface. We further demonstrated a strong spectral and position dependence of the hot electron generation on the placement of the emitter. In particular, the resonance significantly favors these effects.

The physical reason behind the efficient energy conversion in our system is that both the exciting source and the nanoresonator have the same dimensionality: They are zero-dimensional and, therefore, highly localized. Experimentally, a zero-dimensional source of radiation is the key element in the field of tip-enhanced spectroscopies, which includes scanning near field optical microscopy (SNOM) [53, 54], hot electron nanoscopy [55], and hot electron tunneling settings [56]. In tip-driven

spectroscopy, electromagnetic fields and the related hot electron excitation processes become strongly confined in small volumes, leading to a strong enhancement of light-matter interaction. Our approach can also be used to investigate coatings with quantum dots or other emitters on resonance-supporting surfaces. The presented study provides a theoretical background for hot electron generation with localized light sources.

ACKNOWLEDGMENTS

F.B. and S.B. acknowledge funding by the Deutsche Forschungsgemeinschaft (DFG, German Research Foun-

ation) under Germany's Excellence Strategy - The Berlin Mathematics Research Center MATH+ (EXC-2046/1, project ID: 390685689) and by the Helmholtz Association within the Helmholtz Excellence Network SOLARMATH (ExNet-0042-Phase-2-3), a strategic collaboration of the DFG Excellence Cluster MATH+ and Helmholtz-Zentrum Berlin. P.L. acknowledges the support from the NOMOS (ANR-18CE24-0026-03) and ISQUAD (ANR-18CE47-0006-04) projects. A.O.G. acknowledges support by the United States-Israel Binational Science Foundation (BSF).

-
- [1] W. L. Barnes, A. Dereux, and T. W. Ebbesen, *Nature* **424**, 824 (2003).
- [2] L. Novotny and N. van Hulst, *Nat. Photonics* **5**, 83 (2011).
- [3] S. Linic, P. Christopher, and D. B. Ingram, *Nat. Mater.* **10**, 911 (2011).
- [4] M. L. Brongersma, N. J. Halas, and P. Nordlander, *Nat. Nanotechnol.* **10**, 25 (2015).
- [5] G. V. Hartland, L. V. Besteiro, P. Johns, and A. O. Govorov, *ACS Energy Lett.* **2**, 1641 (2017).
- [6] Y. Kim, J. G. Smith, and P. K. Jain, *Nat. Chem.* **10**, 763 (2018).
- [7] N. Wu, *Nanoscale* **10**, 2679 (2018).
- [8] J. S. DuChene, G. Tagliabue, A. J. Welch, W.-H. Cheng, and H. A. Atwater, *Nano Lett.* **18**, 2545 (2018).
- [9] E. Pensa, J. Gargiulo, A. Lauri, S. Schlücker, E. Cortés, and S. A. Maier, *Nano Lett.* **19**, 1867 (2019).
- [10] L. Mascaretti and A. Naldoni, *J. Appl. Phys.* **128**, 041101 (2020).
- [11] Y. Zhang, S. He, W. Guo, Y. Hu, J. Huang, J. R. Mulcahy, and W. D. Wei, *Chem. Rev.* **118**, 2927 (2018).
- [12] H. Harutyunyan, A. B. F. Martinson, D. Rosenmann, L. K. Khorashad, L. V. Besteiro, A. O. Govorov, and G. P. Wiederrecht, *Nat. Nanotechnol.* **10**, 770 (2015).
- [13] M. E. Sykes, J. W. Stewart, G. M. Akselrod, X.-T. Kong, Z. Wang, D. J. Gosztola, A. B. F. Martinson, D. Rosenmann, M. H. Mikkelsen, A. O. Govorov, and G. P. Wiederrecht, *Nat. Commun.* **8**, 986 (2017).
- [14] Y. Negrín-Montecelo, M. Comesaña Hermo, L. K. Khorashad, A. Sousa-Castillo, Z. Wang, M. Pérez-Lorenzo, T. Liedl, A. O. Govorov, and M. A. Correa-Duarte, *ACS Energy Lett.* **5**, 395 (2020).
- [15] B. Hecht, B. Sick, U. P. Wild, V. Deckert, R. Zenobi, O. J. F. Martin, and D. W. Pohl, *J. Chem. Phys.* **112**, 7761 (2000).
- [16] P. Anger, P. Bharadwaj, and L. Novotny, *Phys. Rev. Lett.* **96**, 113002 (2006).
- [17] P. Senellart, G. Solomon, and A. White, *Nat. Nanotechnol.* **12**, 1026 (2017).
- [18] N. C. Lindquist, P. Nagpal, K. M. McPeak, D. J. Norris, and S.-H. Oh, *Rep. Prog. Phys.* **75**, 036501 (2012).
- [19] M. Liu, T.-W. Lee, S. K. Gray, P. Guyot-Sionnest, and M. Pelton, *Phys. Rev. Lett.* **102**, 107401 (2009).
- [20] V. Giannini, A. I. Fernández-Domínguez, S. C. Heck, and S. A. Maier, *Chem. Rev.* **111**, 3888 (2011).
- [21] P. Lalanne, W. Yan, K. Vynck, C. Sauvan, and J.-P. Hugonin, *Laser Photonics Rev.* **12**, 1700113 (2018).
- [22] M. Zworski, *Notices Amer. Math. Soc.* **46**, 319 (1999).
- [23] P. Lalanne, W. Yan, A. Gras, C. Sauvan, J.-P. Hugonin, M. Besbes, G. Demésy, M. D. Truong, B. Gralak, F. Zolla, A. Nicolet, F. Binkowski, L. Zschiedrich, S. Burger, J. Zimmerling, R. Remis, P. Urbach, H. T. Liu, and T. Weiss, *J. Opt. Soc. Am. A* **36**, 686 (2019).
- [24] H. S. Sehmi, W. Langbein, and E. A. Muljarov, *Phys. Rev. B* **95**, 115444 (2017).
- [25] M. Garcia-Vergara, G. Demésy, and F. Zolla, *Opt. Lett.* **42**, 1145 (2017).
- [26] P. B. Johnson and R. W. Christy, *Phys. Rev. B* **6**, 4370 (1972).
- [27] J. Pomplun, S. Burger, L. Zschiedrich, and F. Schmidt, *Phys. Status Solidi B* **244**, 3419 (2007).
- [28] P.-I. Schneider, N. Srocka, S. Rodt, L. Zschiedrich, S. Reitzenstein, and S. Burger, *Opt. Express* **26**, 8479 (2018).
- [29] C. Sauvan, J.-P. Hugonin, I. S. Maksymov, and P. Lalanne, *Phys. Rev. Lett.* **110**, 237401 (2013).
- [30] P. J. Feibelman, *Phys. Rev. B* **9**, 5077 (1974).
- [31] K.-D. Tsuei, E. W. Plummer, and P. J. Feibelman, *Phys. Rev. Lett.* **63**, 2256 (1989).
- [32] G. V. Hartland, *Chem. Rev.* **111**, 3858 (2011).
- [33] L. Genzel, T. P. Martin, and U. Kreibig, *Z. Phys. B* **21**, 339 (1975).
- [34] U. Kreibig and M. Vollmer, *Optical Properties of Metal Clusters* (Springer, Berlin, 1995).
- [35] W. A. Kraus and G. C. Schatz, *J. Chem. Phys.* **79**, 6130 (1983).
- [36] J. Lermé, *J. Phys. Chem. C* **115**, 14098 (2011).
- [37] A. V. Uskov, I. E. Protsenko, N. A. Mortensen, and E. P. O'Reilly, *Plasmonics* **9**, 185 (2014).
- [38] E. Y. Santiago, L. V. Besteiro, X.-T. Kong, M. A. Correa-Duarte, Z. Wang, and A. O. Govorov, *ACS Photonics* **7**, 2807 (2020).
- [39] A. O. Govorov, H. Zhang, and Y. K. Gun'ko, *J. Phys. Chem. C* **117**, 16616 (2013).
- [40] J. M. Ziman, *Principles of the Theory of Solids*, 2nd ed. (Cambridge University Press, 1972).
- [41] D. B. Tanner, *Optical Effects in Solids* (Cambridge University Press, 2019).

- [42] I. Tamm and S. Schubin, *Z. Phys.* **68**, 97 (1931).
- [43] A. M. Brodskii and Y. Y. Gurevich, *Sov. Phys. - JETP* **27**, 114 (1968).
- [44] I. E. Protsenko and A. V. Uskov, *Phys.-Usp.* **55**, 508 (2012).
- [45] S. V. Zhukovsky, V. E. Babicheva, A. V. Uskov, I. E. Protsenko, and A. V. Lavrinenko, *Plasmonics* **9**, 283 (2014).
- [46] A. M. Brown, R. Sundararaman, P. Narang, W. A. Goddard, and H. A. Atwater, *ACS Nano* **10**, 957 (2016).
- [47] L. V. Besteiro, X.-T. Kong, Z. Wang, G. Hartland, and A. O. Govorov, *ACS Photonics* **4**, 2759 (2017).
- [48] C. Kittel, *Introduction to Solid State Physics*, 8th ed. (Wiley, New York, 2005).
- [49] G. Ford and W. Weber, *Phys. Rep.* **113**, 195 (1984).
- [50] A. Sousa-Castillo, M. Comesaña Hermo, B. Rodríguez-González, M. Pérez-Lorenzo, Z. Wang, X.-T. Kong, A. O. Govorov, and M. A. Correa-Duarte, *J. Phys. Chem. C* **120**, 11690 (2016).
- [51] O. A. Baturina, A. Epshteyn, B. S. Simpkins, N. Bhattarai, T. H. Brintlinger, E. Y. Santiago, and A. O. Govorov, *J. Electrochem. Soc.* **166**, H485 (2019).
- [52] L. K. Khorashad, L. V. Besteiro, M. A. Correa-Duarte, S. Burger, Z. M. Wang, and A. O. Govorov, *J. Am. Chem. Soc.* **142**, 4193 (2020).
- [53] H. Heinzelmann and D. W. Pohl, *Appl. Phys. A* **59**, 89 (1994).
- [54] J. Chen, M. Badioli, P. Alonso-González, S. Thongrattanasiri, F. Huth, J. Osmond, M. Spasenović, A. Centeno, A. Pesquera, P. Godignon, A. Zurutuza Elorza, N. Camara, F. J. G. de Abajo, R. Hillenbrand, and F. H. L. Koppens, *Nature* **487**, 77 (2012).
- [55] A. Giugni, B. Torre, M. Allione, G. Das, Z. Wang, X. He, H. N. Alshareef, and E. Di Fabrizio, *Adv. Opt. Mater.* **5**, 1700195 (2017).
- [56] X. Wang, K. Braun, D. Zhang, H. Peisert, H. Adler, T. Chassé, and A. J. Meixner, *ACS Nano* **9**, 8176 (2015).